Measurement report: Sources, sinks and lifetime of NO_x in a sub-urban temperate forest at night

Simone T. Andersen[1], Max R. McGillen[2], Chaoyang Xue[2], Tobias Seubert[1], Patrick Dewald[1], Gunther N. T. E. Türk[1], Jan Schuladen[1], Cyrielle Denjean[3], Jean-Claude Etienne[3], Olivier Garrouste[3], Marina Jamar[4], Sergio Harb[5], Manuela Cirtog[5], Vincent Michoud[6], Mathieu Cazaunau[5], Antonin Bergé[5], Christopher Cantrell[5], Sebastien Dusanter[4], Bénédicte Picquet-Varrault[5], Alexandre Kukui[7], Abdelwahid Mellouki[2,8], Lucy J. Carpenter[9], Jos Lelieveld[1], John N. Crowley[1]

[1]Atmospheric Chemistry Department, Max-Planck-Institute for Chemistry, 55128-Mainz, Germany

[2]Institut de Combustion, Aérothermique, Réactivité Environnement (ICARE), CNRS, 1C Avenue de la Recherche Scientifique, CEDEX 2, 45071 Orléans, France

[3]CNRM, Universite de Toulouse, Meteo-France, CNRS, Toulouse, France

[4]IMT Nord Europe, Institut Mines-Télécom, Université de Lille, Center for Energy and Environment, 59000 Lille, France

[5]Univ Paris Est Creteil and Université de Paris Cité, CNRS, LISA, F-94010 Créteil, France

[6]Université Paris Cité and Univ Paris Est Creteil, CNRS, LISA, F-75013 Paris, France

[7]Laboratoire de Physique et Chimie de l'Environnement et de l'Espace (LPC2E), CNRS Orléans, France

[8]University Mohammed VI Polytechnic (UM6P), Lot 660, Hay Moulay Rachid Ben Guerir, 43150, Morocco

[9]Wolfson Atmospheric Chemistry Laboratory, Department of Chemistry, University of York, York, UK

Correspondence to: Simone T. Andersen (simone.andersen@mpic.de) and John N. Crowley (john.crowley@mpic.de)

1   Abstract

The budget of reactive nitrogen species, which play a central role in atmospheric chemistry (e.g. in photochemical O_3 production), is poorly understood in forested regions. In this study, through observations of NO, NO_2, NO_y and O_3 in the Rambouillet forest near Paris, France, we have examined nighttime processes controlling NO_x in an anthropogenically impacted forest environment. O_3 mixing ratios displayed a strong diel profile at the site, which was driven by a variable but generally rapid deposition to soil and foliar surfaces. The O_3 diel profile was strongly influenced by relative humidity and temperature inversion. Only when the O_3 mixing ratio was sufficiently low (and thus the NO lifetime sufficiently long), were sustained NO peaks observed above the instrumental detection limit, enabling derivation of average NO emission rates from the soil of ~1.4 ppbv h^{-1}. Observations of the lack of increase in NO_2 at night, despite a significant production rate from the reaction of NO with O_3, enabled an effective lifetime of NO_2 of ~0.5-3 h to be derived. As the loss of NO_2 was not compensated by the formation of gas- or particle-phase reactive nitrogen species it was presumably driven by deposition to soil and foliar surfaces, or any products formed were themselves short-lived with respect to deposition. By comparison, the daytime lifetime of NO_2 with respect to loss by reaction with OH is about 1 day. Our results indicate that the nighttime deposition of NO_2 is a major sink of boundary layer NO_x in this temperate forest environment.

2   Introduction

Nitrogen oxides (NO_x = NO + NO_2) are pollutant trace gases, which play a key role in the atmosphere by producing or destroying tropospheric ozone (O_3), which can cause respiratory illness (Ciencewicki and Jaspers, 2007) and damage to plants (Emberson et al., 2018). Photolysis of nitrogen dioxide (NO_2) (R1) is the primary source of tropospheric ozone (O_3), and the nitric oxide (NO) product is oxidized back to NO_2 either by O_3 (R2) or by organic peroxy radicals (RO_2, under formation of alkoxy radicals (RO)) or hydroperoxyl radicals (HO_2) (R3, R4) (Lightfoot et al., 1992). The latter results in formation of the hydroxyl radical (OH) radical, and R3 and R4 thus represent routes to recycle the most important atmospheric radical initiator of oxidation (Hens et al., 2014). It is, therefore, essential to understand the sources and sinks of NO_x in the atmosphere.

$$NO_2 + hv \, (+O_2) \rightarrow NO + O_3 \qquad\qquad\qquad\qquad (R1)$$

$$NO + O_3 \rightarrow NO_2 + O_2 \qquad\qquad\qquad\qquad\qquad (R2)$$

$$NO + RO_2 \rightarrow NO_2 + RO \qquad\qquad\qquad\qquad\quad (R3)$$

$$NO + HO_2 \rightarrow NO_2 + OH \qquad\qquad\qquad\qquad\quad (R4)$$

The dominant global sources of NO_x are anthropogenic in the form of combustion of fossil fuels and to a lesser degree biomass burning and agricultural soils. The natural sources, which include

63 lightning (Schumann and Huntrieser, 2007), wildfires (Val Martin et al., 2008), and unperturbed
64 soil emissions from microbial activities (Davidson and Kingerlee, 1997), are important in regions
65 remote from anthropogenic sources. NO_2 and NO both react with peroxy radicals in the atmosphere
66 to produce organic nitrates (R5-R6), including peroxy nitrates (RO_2NO_2) and alkyl nitrates
67 ($RONO_2$), which are important precursors for the formation of secondary organic aerosols (SOA)
68 (Hallquist et al., 2009; Kanakidou et al., 2005; Kiendler-Scharr et al., 2016). NO_2 also reacts with
69 OH radicals, O_3 and nitrate radicals (NO_3) to form nitric acid (HNO_3) (R7), NO_3 radicals (R8), and
70 dinitrogen pentoxide (N_2O_5) (R9), respectively. N_2O_5 is in thermal equilibrium with NO_2 and NO_3
71 and can interact with aqueous aerosol or moist surfaces to form HNO_3 (R10) (Kane et al., 2001)
72 or nitryl chloride ($ClNO_2$) (Phillips et al., 2013; Phillips et al., 2012). Organic nitrates, SOA, and
73 HNO_3 are all removed from the boundary layer through dry and wet deposition which thereby
74 removes NO_x from the atmosphere.

75 $NO_2 + RO_2 + M \rightarrow RO_2NO_2 + M$ (R5)

76 $NO + RO_2 + M \rightarrow RONO_2 + M$ (R6)

77 $NO_2 + OH + M \rightarrow HNO_3 + M$ (R7)

78 $NO_2 + O_3 \rightarrow NO_3 + O_2$ (R8)

79 $NO_2 + NO_3 + M \rightleftharpoons N_2O_5 + M$ (R9)

80 $N_2O_5 + H_2O \text{ (aq)} \rightarrow 2 HNO_3 \text{ (aq)}$ (R10)
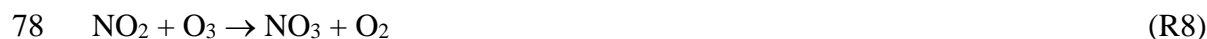
81 In the planetary boundary layer, NO_2 is also lost through dry deposition to surfaces such as soil
82 and leaves. Deposition takes places both at nighttime and daytime, but is expected to be more
83 efficient during daytime due to increased mixing through turbulence. When NO_2 deposits onto
84 humid surfaces, it can lead to the production of nitrous acid (HONO), which can be released to the
85 atmosphere (Meusel et al., 2016; Elshorbany et al., 2012). NO_2 uptake on leaves takes place
86 through stomatal and non-stomatal processes, which have been reported to depend on multiple
87 factors such as stomata aperture and relative humidity. Stomatal uptake primarily occurs at
88 daytime when the stomata are open, leading to increased NO_2 loss compared to nighttime, when
89 the stomata are not fully open (Delaria et al., 2020; Delaria et al., 2018; Chaparro-Suarez et al.,
90 2011). Non-stomatal uptake occurs through the cuticles, though the importance of cuticular uptake
91 has been reported to be small compared to the stomatal uptake (Delaria and Cohen, 2020; Delaria
92 et al., 2020). NO_2 uptake to leaves is reported to be enhanced in the presence of water films, which
93 may exist when the relative humidity is >70% (Thoene et al., 1996; Weber and Rennenberg, 1996;
94 Burkhardt and Eiden, 1994). There is, however, no consensus on this process, as other studies have
95 not observed this effect (Gessler et al., 2000). Most recent work shows that the interactions with
96 foliar surfaces is uni-directional, i.e. emissions are negligible (Delaria et al., 2020).

97 At nighttime, NO_2 photolysis ceases and as a consequence, in the absence of combustion sources,
98 the main sources of NO are emissions from soils (Jaeglé et al., 2005). Since NO is oxidised
99 efficiently by O_3 at night, its concentration will be highest at the surface and will decrease with
100 altitude. The vertical profile of O_3 is the opposite owing to its physical loss due to deposition near

101   the surface and through chemical reaction with NO and/or alkenes combined with entrainment
102   from the nocturnal residual layer. As NO_2 is produced from the reaction between NO and O_3, its
103   vertical gradient is expected to be weaker than those of NO and O_3 (Geyer and Stutz, 2004; Stutz
104   et al., 2004).

105   In this study we use measurements from the ACROSS (Atmospheric ChemistRy Of the Suburban

106   foreSt) campaign to investigate the nighttime sources and sinks of NO_x in a temperate forest. O_3

107   measurements are used to explain the observed NO features and measurements of NO_2 and total

108   gas-phase nitrogen species (NO_y) and particulate nitrate are used to investigate the lifetime and

109   fate of NO_x in the forest environment.

110

111   **3   The ACROSS Campaign**

112   The ACROSS campaign (13th of June 2022 to 25th of July 2022) was conducted in multiple
113   locations in and around Paris, France (Cantrell and Michoud, 2022). Here we present
114   measurements from the Rambouillet forest supersite located approximately 50 km southwest of
115   Paris (48.687, 1.704). The forest consists of approximately 70% oak, 20% pine, and small
116   contributions from beech and chestnut. The top of the forest canopy around the supersite was
117   around 20-25 m. Several instrumented containers were placed in a clearing (~697 m^2) together
118   with a 41 m measurement tower. Most of the instruments used in this study were located in two
119   different containers (MPIC and Orléans). The sampling inlets of the two containers were
120   approximately 17 m apart and the tower was approximately 9 m from the MPIC container and 16
121   m from the Orléans container. The soil measurements were carried out at the bottom of the tower,
122   approximately 13 m from the MPIC container and approximately 17 m from the Orleans container.
123   All the instruments used in this study are described briefly below.

124

125   **3.1   Measurements**

126   **3.1.1   Ground**

127   NO_2 was measured using two different cavity ringdown spectroscopy (CRDS) instruments with
128   co-located inlets sampling from a high-volume-flow stainless steel tube ($10\,m^3\,min^{-1}$; 15 cm
129   diameter, 0.2 s residence time) taking air from a height of 5.4 m above ground. One of the
130   instruments (5CH-CRDS) consists of 3 cavities operated at 408 nm to measure NO_2 and, via their
131   thermal dissociation to NO_2, total peroxy nitrates ($\sum$PNs, 448 K) and total alkyl nitrates ($\sum$ANs,
132   648 K). Two additional cavities, operated at 662 nm, measured NO_3 and (via thermal dissociation
133   to NO_3, 373 K) N_2O_5 (Sobanski et al., 2016). During this campaign, the NO_2 cavity had a limit of
134   detection (LOD) of 9.7 pptv for 1 min averaging (3σ). The second instrument (k-NO3) primarily
135   measures the NO_3 reactivity, but also has a cavity operated at 405 nm for the measurement of NO_2
136   (Liebmann et al., 2018).

137   Another CRDS instrument was used to measure NO_x, NO_y, and particulate nitrate (pNO_3) from

138   co-located inlets near the high-volume-flow stainless steel tube. NO_x was measured by adding O_3

139   to the ambient sample, thereby oxidizing NO to NO_2, which was measured with CRDS at 405 nm

140   (Friedrich et al., 2020). A judicious choice of O_3 and reaction time ensured that minimal (>1%) of

141   NO_2 was oxidized to NO_3. At times with low (or zero) NO, NO_x concentrations were in close

142   agreement with both NO_2 measurements. NO_y was measured by passing ambient air through a

143   quartz inlet at ~ 900 K which quantitatively converts reactive nitrogen trace-gases to NO or NO_2.

144   Exceptions are N_2O, HCN and NH_3, which are not detected. In this location, NO_y is expected to

145   consist mainly of NO_x + NO_3 + N_2O_5 + HNO_3 + PNs + ANs + HONO + $ClNO_2$ + particulate

146   nitrates (pNO_3).

147   Particulate nitrates (both organic and inorganic) were separately measured (as NO_y) after denuding

148   gas-phase reactive nitrogen species (Friedrich et al., 2020). To achieve this, problems involving

149   the ineffective trapping of gas-phase NO_x by the denuder was eliminated, as will be described in

150   a forthcoming technical paper.

151   O_3 was measured from the high-volume-flow stainless-steel tube with a commercial instrument

152   (2B Technologies model 205) using UV absorption at 254 nm. The LOD is 2 ppbv for 10 s

153   averaging time.

154   A spectral radiometer (metcon Gmbh) was installed near the co-located inlets on top of the MPIC

155   container to measure actinic fluxes, which were used to calculate photolysis frequencies as

156   described elsewhere (Meusel et al., 2016).

157   NO was measured from the Orléans container using a commercial chemiluminescence instrument

158   (Ecophysics CLD 780 TR, henceforth CLD) with an LOD of 10 pptv for 1 min averaging time.

159   The sampling height for NO measurements was about 0.6 and 3.2 m above the container top and

160   the ground surface, respectively. The NO measurements required correction due to a change in the

161   CLD sensitivity during the campaign caused by an interruption in the instrument's oxygen supply.

162   The corrections and the corrective procedure are described in the SI.

163   HONO was measured by a commercial long-path absorption photometer (LOPAP-03, QUMA

164   GmbH, Germany) with a sampling height of 2.0 m above the ground level. Details about the

165   LOPAP instrument can be found elsewhere (Heland et al., 2001; Kleffmann et al., 2006). During

166   the campaign, the LOPAP was calibrated by diluted nitrite when changing any supporting

167   solutions. Zero calibration by measuring synthetic air was conducted 2-3 times per day. The

168   detection limit is < 5 pptv.

169   The sum of peroxy radicals, XO_2=HO_2+RO_2, was measured by their conversion to H_2SO_4 in

170   presence of NO and SO_2 and detection of the generated H_2SO_4 using NO_3^- CIMS (Kukui et al.,

171   2008). The calibration coefficient is determined using N_2O actinometry and OH/RO_2 generation

172   in a turbulent flow reactor by photolysis of N_2O or H_2O at 184.9 nm. The calibration of HO_2,

173   CH_3O_2 and other RO_2 is performed by adding into the calibration reactor CO, CH_4 (or other RO_2

174 precursors) converting OH to RO$_2$. The overall estimated calibration accuracy (2σ) for XO$_2$ is
175 about 30%, although the uncertainty of the XO$_2$ measurements is typically higher due to
176 uncertainty in ambient air XO$_2$ composition. The lower limit of detection for XO$_2$ radicals at S/N=3
177 and a 4 minute integration time is 2×10^6 molecule cm^{-3}.

178 Time series of the most relevant measurements can be found in Figure S1-2. Due to missing total
179 NO$_x$ and NO$_y$ measurements prior to June 25th and NO after July 18th, the data analysis is focused
180 on the time period in between these dates.

181

182 3.1.2   Tower
183 Measurements at 41 m were conducted with instruments located on the tower as well as through a
184 manifold with an inlet at the top of the tower. The manifold was built from glass tubing (4.9 cm
185 inner diameter, Borodrain) with a residence time in the manifold of 2.1 s. NO$_2$ was measured using
186 a cavity attenuated phase shift (CAPS) instrument on the tower with an LOD of 40 pptv, which
187 was zeroed every 1-2 hours. NO and O$_3$ were both measured from the manifold using a
188 chemiluminescence instrument with a LOD of 30 pptv and a HORIBA (APOA370) with an LOD
189 of 2.5 ppbv, respectively. The NO measurements were corrected for losses due to the reaction of
190 NO with O$_3$ in the manifold and the sampling line (total 5.5 s), with corrections ranging from 1-
191 28%. Time series of all three measurements are plotted in Figure S3.

192

193 3.1.3   Meteorology and Soil
194 Ambient temperature was measured at four different heights on the tower; 5 m, 13 m, 21 m, and
195 41 m using temperature sensors from Atexis (PT1000) and Thermoest (PT100). Relative humidity
196 was measured at 5 m using a Vaisala humidity sensor (HMP45A). Soil temperature and moisture
197 were measured at 5 cm, 10 cm, and 30 cm below the surface using probes from Thermoest (PT100)
198 and Delta T (Thetaprobe ML2X), respectively. Wind speed and direction were measured at 41 m
199 using a wind monitor from Young Company. Time series of all the meteorological and soil
200 measurements are shown in Figure S4-5.

201

202 3.2   HYSPLIT
203 To identify different air masses, 48-hour back trajectories were simulated every hour at a
204 terminating height of 40 m using the Hybrid Single-Particle Lagrangian Integrated Trajectory
205 model (HYSPLIT, version 4, 2019) (Draxler and Rolph, 2011). The back-trajectories were
206 modelled using meteorological data from the Global Data Assimilation System (GDAS) at a
207 resolution of 1 degree. This led to the separation of the data into two periods, 25th of June to 2nd of
208 July and 3rd of July to 18th of July, which are plotted in Figure 1. The first phase is dominated by
209 clean air from over the Atlantic Ocean (henceforth called "Atlantic"). Back trajectories indicated
210 that the vast majority of air masses were transported within the boundary layer prior to reaching
211 the site and thus may have reasonably fresh "marine influence". The second phase is dominated

212 by air that has passed over urban locations including Paris, Brussels and the Ruhr area within the
213 last 48 hours (henceforth called "Continental").

214

215 **4   Results and Discussion**
216 Two 24-hour periods of temperature (at 4 different heights), NO, O_3, relative humidity (RH), NO_2,
217 and NO_2 photolysis rate constant (JNO_2) are plotted in Figure 2. The left panels show 24 hours
218 with Atlantic air and the right panels 24 hours with continental air. Immediately apparent in these
219 datasets (and in Fig S1) is the large diel cycle in O_3 mixing ratios, with net daytime production
220 resulting in mid-afternoon mixing ratios between ~30 and 90 ppbv. In contrast, very low O_3 mixing
221 ratios (often approaching zero) were observed at nighttime.

222 In the lowermost panels (JNO_2 measurements), the nighttime is shown in dark grey and the two
223 light grey areas show the time before sunset (about 5 hours) and after sunrise (about 4.5 hours)
224 when very little direct sunlight reaches the ground of the site due to shading by the trees. This
225 leaves about 6.5 hours centred around midday when direct sunlight reaches the ground. The
226 shading results in radiative cooling of the ground in the late afternoon and associated temperature
227 inversions begin to form prior to sunset as can be observed in the right panels of Figure 2 and in
228 more detail in Figure S6. The temperature inversions begin approximately at the same time as the
229 ground temperature at 5 cm below the surface starts to decrease (see Figure S6). These conditions
230 of insolation were relatively consistent throughout the campaign.

231 Clear temperature inversions were observed for both nights shown in Figure 2, the beginning and
232 end of which are indicated by dashed lines. Vertical mixing can be reduced significantly during a
233 temperature inversion, which is apparent from the O_3 and RH measurements in the right-hand
234 panel. In both examples, O_3 decreases at the ground level (5.4 m) at the beginning of the
235 temperature inversion and increases as the inversion breaks down in the morning. This behaviour
236 is understood in terms of O_3 loss to soil surfaces and through stomatal and non-stomatal uptake on
237 leaves (Zhou et al., 2017; Rannik et al., 2012; Altimir et al., 2006; Ganzeveld and Lelieveld, 1995)
238 as well as through chemical reactions with e.g. NO, NO_2 and unsaturated (biogenic) organics
239 (Kurpius and Goldstein, 2003). Reduced vertical mixing means that during the inversion, O_3 is
240 only slowly replenished by downward mixing of air masses above the canopy where higher O_3
241 levels are observed. In contrast, the RH behaves in the opposite sense as the air above the inversion
242 is drier than close to the ground, where evapotranspiration contributes to enhanced water vapour
243 concentrations.

244 If the only source of NO was the photolysis of NO_2, NO mixing ratios would be expected to follow
245 the NO_2 photolysis rate during the day and tend to zero at night as NO is oxidized on a time scale
246 of minutes (for $O_3 > 10$ ppb) to NO_2 by O_3. This was not always the case during ACROSS. A
247 pronounced NO peak (up to ~2 ppbv) was observed at ground level between 00:00 and 06:00 UTC
248 (02:00 and 08:00 local time) during the phase dominated by Atlantic air, shown in Figure 2, which
249 is absent in the phase dominated by continental air. The peak occurs prior to sunrise and is only
250 observed by the ground-level measurements suggesting a non-photolytic source of NO close to the
251 ground, which is discussed further below. Very low (0-5 ppbv) O_3 mixing ratios coincide with the

252   sustained nighttime NO peak observed, which is never reached in the example from the continental
253   phase, although in both cases clear temperature inversions were seen. Additional examples of
254   sustained NO peaks (i.e. lasting several hours at level between 1 and 2 ppbv) at night during the
255   first phase are shown in Figure S7. Examples of additional nights with temperature inversions
256   during phase 2, where NO mixing ratios remained close to zero, are shown in Figure S8.

257

258   ## 4.1   Nighttime Ozone Loss
259   For each night between June 17th and July 22nd the net O_3 loss rate constant, $k_L(O_3)$ was derived
260   by fitting exponential expressions to the data for periods of 4.5 to 8 hours. $k_L(O_3)$ was highly
261   variable, with values between 1.8×10^{-5} s^{-1} and 3.0×10^{-4} s^{-1}, depending on the strength of the
262   temperature inversion and the relative humidity (see discussion below). These values of $k_L(O_3)$
263   correspond to lifetimes of 1-15 hours for O_3 at nighttime. Chemical losses of O_3 occur through
264   reactions with NO, NO_2, and unsaturated BVOCs (Zhou et al., 2017). Rate coefficients of reactions
265   of O_3 with NO (1.9×10^{-14} cm^3 molecule^{-1} s^{-1} at 298 K), NO_2 (3.5×10^{-17} cm^3 molecule^{-1} s^{-1} at 298
266   K), limonene (a reactive terpene, 2.2×10^{-16} cm^3 molecule^{-1} s^{-1} at 298 K), β-caryophyllene
267   (sesquiterpene, 1.2×10^{-14} cm^3 molecule^{-1} s^{-1} at 298 K) are low such that mixing ratios in excess
268   of 1 ppbv for NO and β-caryophyllene would be required to explain the O_3 loss rate constant
269   (IUPAC, 2024). Required mixing ratios of terpenes or NO_2 would be even larger (60-300 ppbv).
270   As such high mixing ratios of NO and NO_2 were not observed continuously and such levels of
271   BVOC are unlikely, we assume that chemical losses of O_3 are insignificant compared to deposition
272   as previously observed (Zhou et al., 2017). Ignoring entrainment from other heights, we can then
273   equate $k_L(O_3)$ to ($2V_d/h$), where V_d is the deposition velocity and h is the boundary layer height;
274   the factor 2 is used to account for a positive vertical gradient (Shepson et al., 1992). Using a
275   boundary layer height of 20 m (arbitrarily set equal to the top of the canopy) gives net deposition
276   velocities varying between 0.018 and 0.3 cm s^{-1}. These values for V_d are in broad agreement with
277   other studies in temperate forests, where deposition velocities for O_3 at nighttime have been
278   reported to be around 0.07-0.3 cm s^{-1} (Padro, 1996, 1993; Finkelstein et al., 2000; Wu et al., 2016).

279   In Figure 3 the O_3 production rate ($JNO_2 \times [NO_2]$), RH, temperature at 4 different heights and O_3
280   mixing ratio have been plotted for two nights with high average RH to illustrate the impact of
281   temperature inversions on the net O_3 loss-rate constants. The production rate of O_3 is used to
282   identify periods in which production is negligible. In the left panel a night without a temperature
283   inversion is plotted, where the average RH for the period used to fit the exponential decay is 93 ±
284   3 %. These conditions resulted in a net O_3 loss-rate constant of 6.0×10^{-5} s^{-1}. In contrast, the night
285   depicted in the right panel has the same average RH (92 ± 3 %) and a very clear temperature
286   inversion, which gives a net O_3 loss-rate constant of 3.0×10^{-4} s^{-1}. This gives a factor of 5 between
287   these two net O_3 loss-rate constants depending on whether a temperature inversion is observed or
288   not. This can be understood in terms of the O_3 being replenished from above when there is no (or
289   a weak) inversion, which is not the case when there is an inversion. Bearing this in mind, the use
290   of $k_L(O_3)$ (a *net* O_3 loss constant) must result in a lower limit to V_d unless strong temperature
291   inversions (preventing O_3 entrainment from above) are present. The O_3 loss rate will also be
292   enhanced under conditions of strong inversion if trace-gases that are reacive towards O_3 are

293 released into a very shallow boundary layer. However, as indicated above, chemical losses are not
294 expected to compete with physical losses.

295 To investigate the impact of RH on the net O_3 loss-rate constants, two nights with temperature
296 inversions are plotted in Figure S9; one with high RH (92 ± 3 %) and one with a lower RH (63 ±
297 6 %). Here we see a large decrease in $k_L(O_3)$ from 3.0×10^{-4} s^{-1} to 4.5×10^{-5} s^{-1}, when going from
298 high to lower RH. The individually determined O_3 loss-rate constants are plotted as a function of
299 RH in Figure 4 and coloured depending on whether a temperature inversion is observed or not
300 during the time period which was used for the exponential decay fit. A clear increase in O_3 loss-
301 rate constants can be observed when RH increases above 70-80% when a temperature inversion
302 was observed. A small increase at RH higher than 70-80% was also observed when temperature
303 inversions were absent. The observed dependence of $k_L(O_3)$ on relative humidity is consistent with
304 previous studies in forested regions, which have reported an increase in O_3 loss above 60-70% RH
305 (Altimir et al., 2006; Rannik et al., 2012; Zhou et al., 2017). Altimir et al. (2006) suggested an
306 enhancement factor which is humidity dependent above 70% RH; 1 at 70% RH, 2 at 85% RH and
307 a sharp increase to over 5 when moving towards 100% RH. In a boreal forest these observations
308 have been explained by the formation of a "wet skin" on leaves which enhances surface O_3 losses
309 by modifying (reducing) the surface-resistance to uptake (Zhou et al., 2017). This is in broad
310 agreement with our observations during nights with a temperature inversion (see Figure 4), and
311 the discrepancies between the studies could be explained e.g. by different tree types, the height of
312 the boundary layer, strength of the inversion and temperature.

313 The faster net rate of O_3 loss on nights with high relative humidity and well-defined temperature
314 inversions explain the differences observed in the O_3 mixing ratios at night during the Atlantic and
315 continental phases. The average nighttime (20:00-04:00 UTC) RH for the Atlantic phase was 87.4
316 ± 7.6 (1σ) % compared to 68.4 ± 12.7 (1σ) % for the continental phase, indicating that on nights
317 with temperature inversions higher loss-rate constants would be expected for the Atlantic phase.
318 The high RH combined with the significantly lower average peak O_3 mixing ratio in the Atlantic
319 phase (34.5 ± 6.0 (1σ) ppbv between 14:00-15:00 UTC) compared to the continental phase (52.7
320 ± 13.6 (1σ) ppbv between 14:00-15:00 UTC) explains why on nights with temperature inversions
321 during the Atlantic phase the O_3 was essentially completely depleted as shown in Figure 2 and S7.

322

323 **4.2   Nitrogen Oxide Soil Emissions**
324 Figure 2 (left panel) and S7 show nighttime periods in which NO was observed when O_3 was
325 depleted during the Atlantic phase. The several hours duration of the period when NO was above
326 the LOD excludes very local combustion as the source, leaving soil emissions resulting from
327 microbial activity (Davidson and Kingerlee, 1997) as the most likely source of NO. At 293 K and
328 2 ppbv of O_3, the lifetime of NO towards reaction with O_3 is around 20 minutes. It is therefore
329 reasonable to assume that NO is close to steady-state when there is 2 ppbv or more of O_3 available.
330 The NO emission rate (E_{NO}) can therefore be equated to the loss rate of NO as described in equation
331 (1) assuming all peroxy radicals (XO_2) react with the same rate coefficient as HO_2:

332 $E_{NO} = k_{NO+O3}[NO][O_3] + k_{NO+HO2}[XO_2][NO]$ (1)

333   where k_{NO+O_3} and k_{NO+HO_2} are the temperature-dependent rate constants for the reaction between
334   NO and O_3 and HO_2, respectively, (IUPAC, 2024) and [NO], [O_3] and [XO_2] are the measured
335   concentrations of NO, O_3 and XO_2, respectively. In Figure 5, NO and E_{NO} (when $O_3 > 2$ ppbv) at
336   nighttime ($JNO_2 < 10^{-5}$ s^{-1}) are separated by air masses and plotted against O_3, where the outliers
337   are defined as being outside $1.5 \times$ interquartile range (IQR). While the nighttime NO mixing ratio
338   increased rapidly when O_3 tended towards 0 ppbv during the Atlantic phase, O_3 was never depleted
339   to less than 5 ppbv during the Continental phase and therefore no sustained periods of enhanced
340   NO were observed at nighttime. In contrast, no significant trend is found when plotting E_{NO} against
341   O_3 for either of the phases, which shows that the calculated soil emission of NO is not dependent
342   on O_3. This indicates that while the soil is an important but variable source of NO, sustained
343   nighttime NO peaks are only observed above the instrument LOD when O_3 is almost totally
344   depleted so that the lifetime of NO is long enough to allow its concentration to build-up
345   sufficiently.

346   Water content and temperature have previously been shown to impact the emission rate of NO
347   from soil (Pilegaard, 2013; Rosenkranz et al., 2006). Rosenkranz et al. (2006) found a positive
348   correlation between soil moisture and NO emission up to 40% water-filled pore space (WFPS) and
349   an optimum between 12.5 and 15 °C soil temperature in a sessile oak forest in Hungary. In Figure
350   6, NO and E_{NO} are plotted against the soil temperature and moisture at 5 cm below the surface.
351   The measured NO mixing ratios peak towards the highest soil moisture and lowest soil temperature
352   measured during this campaign, however, as with O_3, there is no significant trend in the NO
353   emission rates with soil moisture. At the low (11.5-12.5 °C) and high (19.5-20.5 °C) nighttime soil
354   temperatures very few measurements were made (around 2 hours combined) compared to the rest
355   of the temperature intervals. Across the remaining temperature intervals, no significant trend was
356   observed in the estimated NO emission.

357   The average NO emission rate derived for the two phases is identical with values of
358   1.45 ± 1.61 ppbv h^{-1} (1σ, median = 1.27 ppbv h^{-1}) and 1.42 ± 5.68 ppbv h^{-1} (1σ, median = 0.71
359   ppbv h^{-1}) for the Atlantic and Continental phases, respectively, when using data where $O_3 > 2$
360   ppbv. The Continental phase show much higher variability resulting from more spikes in the data
361   during that period. When O_3 is completely depleted during the Atlantic phase, the increase in NO
362   per hour results in NO emission rates of 0.3-1.8 ppbv h^{-1}, which is in reasonable agreement with
363   the averages across each of the two phases when there is still O_3 present. By assuming a mixed
364   nocturnal boundary layer (NBL) with a height of 20 m (top of the canopy), the average emission
365   rates can be converted to NO emission fluxes of 16.6 ± 18.5 (1σ) and 16.2 ± 65.0 (1σ) µg N m^{-2} h^{-1}
366   , respectively. These values are within the range of previous measurements in different European
367   forests with similar tree types to those found in the Rambouillet forest (see Table 1). The
368   measurements by Pilegaard et al. (2006) and Rosenkranz et al. (2006) were all performed using
369   the chamber technique, whereas Schindlbacher et al. (2004) measured the emission from soil
370   samples collected in the field and exposed to different temperatures and humidity in the laboratory.
371   The chamber-derived emission rates are all either lower or, within combined uncertainties, equal
372   to the values determined in this study, while emission rates from the soil samples were higher than
373   (or, within combined uncertainties, equal to) the values derived in the present study. Davidson and
374   Kingerlee (1997) modelled the global NO emission inventory from soil depending on the biome

375 (e.g. temperate forest, agriculture, and savanna), and split the temperate forest category into
376 regions affected by nitrogen deposition or not. For temperate forests not affected by nitrogen
377 deposition, those authors estimated a flux of 0.0-0.2 kg N ha^{-1} yr^{-1} (0.0-2.3 µg N m^{-2} h^{-1}), which is
378 in good agreement with the lower measurements by Pilegaard et al. (2006). In contrast, the
379 temperate forests impacted by nitrogen deposition had estimated fluxes of 1.1-5.0 kg N ha^{-1} yr^{-1}
380 (12.6-57.1 µg N m^{-2} h^{-1}), which is in good agreement with our measurements at Rambouillet where
381 nitrogen deposition is enhanced by pollution arriving from Paris and other surrounding urbanized
382 / industrialized areas. While noting that our fluxes are broadly consistent with previous
383 measurements, we recognise that the calculations are based on the assumptions of a well-mixed
384 boundary layer of fixed height arbitrarily set at 20 m and should not be over-interpreted.

385

386 **4.3   Nitrogen Dioxide Losses**
387 At nighttime, in the absence of its photolysis, NO_2 may be expected to increase in concentration
388 (via R2) when a constant NO source exists (e.g. from soil, as observed here) and when O_3 is
389 present. For both the Atlantic and the Continental phases an average diel profile between 20.00
390 and 04.00 UTC of NO_2 (black) is plotted in Figure 7. No obvious increase in NO_2 can be observed
391 in the Atlantic phase and an average increase of around 1 ppbv can be observed in the Continental
392 phase. The expected NO_2 resulting from the NO + O_3 reaction if there were no loss mechanisms
393 of NO_2 is plotted in red. This is determined using the NO_2 measured at 20.00 UTC and
394 incrementing this value by the NO_2 that would have been produced through NO oxidation by O_3
395 and peroxy radicals in each time step. In both phases, the simple assumption of nighttime NO_2
396 production through NO + O_3 and NO + XO_2 and no NO_2 loss results in significant generation of
397 NO_2 with an overestimation of 10-12 ppbv of NO_2 at the end of the night compared to the measured
398 NO_2. A loss mechanism of around 1.4 ppbv h^{-1} of NO_2 is therefore necessary to explain the
399 observed (lack of increase in) NO_2.

400

401 **4.3.1   Chemical Losses**
402 While during the daytime NO_2 is removed in a largely irreversible process through reaction with
403 OH radicals to form HNO_3, this is unlikely to represent a significant sink at nighttime. In the
404 absence of photochemical formation pathways, OH is generated at night in the ozonolysis of
405 olefins and in the reaction of HO_2 with NO_3 and NO.

406 O_3 + >=< $\rightarrow$ $\rightarrow$ OH   (R11)

407 $NO_3 + HO_2 \rightarrow OH + NO_2 + O_2$ (R12)

408 $NO + HO_2 \rightarrow OH + NO_2$ (R4)

409 In the forested environment in summer, the emissions of biogenic volatile organic compounds
410 (BVOC) (e.g. olefinic terpenoids) will favour R11 and simultaneously disfavour R12 as NO_3 will
411 be reduced in concentration through its reactions with BVOCs. During the ACROSS campaign
412 ground NO_3 levels were generally below instrument detection limits of 2 pptv and we can
413 reasonably ignore R12. Measurements of OH in forested environments are sparse, though they

414   indicate that nocturnal OH levels are low, with concentrations generally lower than 1×10^5
415   molecule cm^{-3}. Combining the rate coefficient for reaction of OH with NO_2 of $\sim 1 \times 10^{-11}$ cm^3
416   molecule^{-1} s^{-1} (IUPAC, 2024) at ambient pressure and $\approx$ 300 K with an upper limit (confirmed by
417   measurements) to the OH concentration of 1×10^6 molecule cm^{-3} results in a NO_2 loss constant of
418   1×10^{-5} s^{-1}, or (at the average nighttime NO_2 = 1650 pptv) a loss rate of ~60 ppt h^{-1}, clearly
419   insufficient to explain the observations.

420   NO_2 is also lost via its reaction with O_3 to form the NO_3 radical (R8). In an upcoming paper, we
421   will show that the majority of NO_3 formed in the forest will react with BVOCs rather than with
422   NO (to re-form NO_2) and, to a good approximation, R8 represents an irreversible loss of NO_2 as
423   the alkyl nitrates will not release nitrogen in the form of NO_2 at nighttime. However, the rate
424   coefficient for this process (3.5×10^{-17} cm^3 molecule^{-1} s^{-1} at 298 K, (IUPAC, 2024)) is very small
425   and with average nighttime O_3 levels reduced by deposition (see above) to 23 ppbv, the lifetime
426   of NO_2 with respect to this reaction is 14 hours and the loss-rate (at the average nighttime NO_2 =
427   1650 pptv) is ~120 pptv h^{-1}, again too slow to contribute significantly to the apparent loss rate of
428   NO_2.

429   The chemical loss of NO_2 via reaction with OH or via formation of NO_3 and its further reactions
430   with BVOC to form alkyl nitrates is expected to result in the conversion of NO_x to NO_y. As
431   described in section 3.1.1, during the ACROSS campaign we operated a NO_y instrument to
432   measure NO_y both in the gas- and particle-phases. Figure 8 displays the average diel profiles of
433   NO_z (NO_y-NO_x) and pNO_3 during the Atlantic and Continental phases. For both NO_z and pNO_3
434   the diel profiles show either a decrease or stable mixing ratio across the period in which losses of
435   10-12 ppbv of NO_2 are required to explain the observations. Clearly, the loss of NO_2 at nighttime
436   is not balanced by the formation of other forms of reactive nitrogen that were long lived enough
437   to be detected. Trace gases such as HNO_3 or alkyl nitrates may be lost via deposition to surfaces,
438   especially at high relative humidity and lifetimes for biogenic alkyl nitrates of a few hours have
439   been reported (Liebmann et al., 2019; Farmer and Cohen, 2008; Browne et al., 2013; Romer
440   Present et al., 2019). However, as shown above, the limiting step in the formation of organic
441   nitrates is the slow reaction of NO_2 with O_3, which will not convert sufficient NO_2 to NO_z to
442   explain our observations. Formation of organic nitrates that do not require the intermediacy of NO_3
443   (i.e. peroxy nitrates formed from $RO_2 + NO_2$) would also have been detected by the NO_y instrument
444   and can thus also be ruled out as major reservoirs of NO_x.

445   NO_2 deposited to humid surfaces can be converted to HONO and released to the atmosphere
446   (Elshorbany et al., 2012; Meusel et al., 2016). A time series of HONO can be found in Figure S2
447   which reveals increases in HONO at nighttime. However, the HONO mixing ratios can account
448   for only a small fraction of the NO_2 loss described above. This may reflect the fact that, if formed
449   at a moist surface, (soluble) HONO is unlikely to desorb quantitatively into the gas-phase. The
450   low HONO mixing ratios measured during the Atlantic phase compared to the Continental phase,
451   could potentially be explained by the difference in soil humidity, however, the factors influencing
452   the formation and release of HONO are complex. The HONO observations will be analysed in
453   detail in a seperate publication from the ACROSS campaign.

454 In the absence of other known gas-phase mechanisms for the removal of NO_2 at night and the fact
455 that very little other reactive nitrogen trace-gases or nitrate particles are formed during the night,
456 we conclude that physical removal of NO_2 (i.e. deposition) is responsible for its lack of build-up
457 at night during ACROSS and that any transformation of NO_2 at the surface does not lead to
458 quantitative release into the gas-phase

459

460 **4.3.2 Physical Losses**
461 NO_2 is known to be lost through dry deposition to surfaces such as soil and leaves, the latter
462 depending on whether the stomata are open (daytime) or not fully open (nighttime) (Delaria et al.,
463 2020; Delaria et al., 2018; Chaparro-Suarez et al., 2011). As for O_3, dry deposition of NO_2 to
464 surfaces can be described by an exponential decay with a first-order decay rate constant, $k_L(NO_2)$
465 $= (V_d/h)$, where V_d is the deposition velocity and h is the boundary layer height. This expression
466 applies when gradients within the boundary layer are weak, as expected for NO_2 (see above) even
467 though vertical mixing is very slow at night. The net production (or loss) of NO_2 is given by Eq.
468 (2) where the first term on the right-hand side is the NO_2 production rate from the reaction of NO
469 with O_3 or XO_2 (which is identical to the NO soil emission rate) and the second term is the loss
470 rate assuming only depositional losses (see above) and ignoring entrainment of NO_2 from other
471 heights. This will give an upper limit of the NO_2 deposition rate as a small fraction (<10%) of NO_2
472 is lost through chemical reactions with O_3 and OH (see above).

473 $$\frac{d[NO_2]}{dt} = E_{NO} - k_L(NO_2)[NO_2]_0 \qquad (2)$$

474 $[NO_2]_0$ is the NO_2 mixing ratio at 20.00 UTC. The NO_2 concentration at any subsequent time can
475 then be calculated as described in Eq. (3) with variation of $k_L(NO_2)$ in order to match the observed
476 NO_2 mixing ratio.

477 $$[NO_2]_t = \int_0^t \frac{d[NO_2]}{dt} + [NO_2]_0 \qquad (3)$$

478 In Figure 7 the grey lines symbolize the calculated NO_2 mixing ratios at nighttime using values of
479 $k_L(NO_2)$ between 1.0×10^{-4} and 4.0×10^{-4} s^{-1}. As expected, no single value of $k_L(NO_2)$ can explain
480 all the measurements as the height of the BL will not be invariant during the whole night. However,
481 for the Continental and Atlantic phases the observed NO_2 can be explained with $k_L(NO_2) = (2.0 \pm$
482 $1.0) \times 10^{-4}$ s^{-1} and $k_L(NO_2) = (2.75 \pm 1.25) \times 10^{-4}$ s^{-1}, respectively, which results in lifetimes of ~
483 1-3 h and ~ 40-110 min for NO_2 at nighttime. As deposition of NO_2 in this environment represents
484 a permanent loss of NO_x from the gas phase, this lifetime can be compared to e.g. the lifetime of
485 NO_x with respect to its conversion to HNO_3 via reaction of NO_2 with OH which is ~ 1 day
486 (assuming average $[OH] = 1 \times 10^6$ molecule cm^{-3}). The low aerosol surface area during ACROSS
487 combined with the low uptake coefficient for NO_2 renders losses due to heterogeneous processes
488 insignificant (IUPAC, 2024). Clearly, only depositional losses of NO_2 in a forested environment
489 contribute substantially to its lifetime at night and to the NO_x budget.

490 If we continue to assume the nocturnal boundary layer at the forest site is at the top of the canopy
491 (20 m), then the NO_2 loss-rate constants we determined can be converted to a deposition velocity
492 of 0.4 ± 0.2 cm s^{-1} and 0.55 ± 0.25 cm s^{-1} for the Continental and Atlantic phase, respectively.
493 These are comparable to previous measurements of NO_2 deposition velocities of 0.15 cm s^{-1}
494 (Dewald et al., 2022), 0.1-0.57 cm s^{-1} (Rondón et al., 1993), 0.098 cm s^{-1} (Breuninger et al., 2013),
495 0.2-0.5 cm s^{-1} (Horii et al., 2004), 0.02-0.64 cm s^{-1} (Puxbaum and Gregori, 1998), for a mountain
496 observatory surrounded by coniferous trees, boreal coniferous forests, a temperate coniferous
497 forest, a temperate mixed deciduous forest, and a temperate oak forest, respectively, where a
498 combination of soil and foliage deposition is measured. Horii et al. (2004) saw an increase in
499 deposition velocity with increasing NO_2 mixing ratio; from 0.2 cm s^{-1} at 1 ppbv to 0.5 cm s^{-1} at 30
500 ppbv. Puxbaum and Gregori (1998) reported monthly averages of 0.02-0.64 cm s^{-1}, however, their
501 nighttime deposition velocities averaged below 0.05 cm s^{-1}. The deposition velocities determined
502 here are a factor of 5-40 higher than what has been measured for nighttime foliage deposition
503 velocities to the leaves of different trees native to California (Delaria et al., 2020; Delaria et al.,
504 2018), but in good agreement with measurements for daytime. It is, however, important to note
505 that the deposition velocities estimated here are upper limits as the estimation of the NO emission
506 rate is an upper limit and chemical loss of NO_2 is not taken into account. Using an average
507 nighttime NO_2 mixing ratio of 1650 and 1450 pptv for the Continental and Atlantic phase,
508 respectively, results in NO_2 deposition rates of 13.6 ± 6.8 µg N m^{-2} h^{-1} and 18.7 ± 8.5 µg N m^{-2} h^{-1}
509 , which are in reasonable agreement with that measured for soil NO_2 deposition in a sessile oak
510 forest of 9.67 ± 1.92 µg N m^{-2} h^{-1} during the summer (Rosenkranz et al., 2006). The estimated NO
511 soil emission rate and NO_2 deposition rate are, within the uncertainties, identical, which means the

512 Rambouillet forest is not a significant direct source or sink of NO_x.

513

5   Conclusions:

515 Measurements of NO, NO_2, NO_y, and O_3 during the ACROSS campaign (June-July 2022) in the
516 Rambouillet forest southwest of Paris, France, have been used to gain insight into nighttime

517 processes controlling NO_x in an anthropogenically impacted forest environment. Based on
518 HYSPLIT back trajectories, two phases of the campaign were identified; one dominated by air
519 originating over the Atlantic Ocean ("Atlantic"), which on average had high relative humidity and
520 low O_3 mixing ratios, and one dominated by continental air masses from different
521 urban/industrialized regions ("Continental"), which on average had a lower relative humidity than
522 the Atlantic phase and higher O_3 mixing ratios. Strong diel profiles were observed in the O_3
523 measurements across the campaign with daytime peak mixing ratios varying from ~30 to 90 ppbv
524 and nighttime tending towards 0-10 ppbv. The daily variation was driven by a variable but
525 generally rapid O_3 deposition to soil and foliar surfaces, with a strong influence of relative
526 humidity (influencing the surface resistance to uptake) and inversion (influencing the rate of
527 entrainment of O_3 from above the canopy).

528 During the Atlantic phase, periods of sustained NO above the instrumental detection limit was
529 observed at nighttime when O_3 was sufficiently low (i.e. the NO lifetime sufficiently long). This

enabled the derivation of an average NO emission rate from the soil (E_{NO}) of ~1.4 ppbv h^{-1}, which was confirmed by the approximately linear increase in NO observed in the absence of O_3 in the Atlantic phase. The estimated E_{NO} is in broad agreement with previous measurements in other European temperate forests with tree types as found in the Rambouillet forest. The uncertainty in the estimated NO emission rate is determined from the uncertainties in NO and O_3 at 3-5 m above ground, which leads to higher relative uncertainties at low NO and O_3 mixing ratios. Measurements of either NO fluxes or highly resolved height profiles of NO and O_3 will improve the NO emission rate estimate during future field campaigns.

An increase in NO_2 at night would be expected when having a constant NO emission rate of ~1.4 ppbv h^{-1} in the presence of O_3 as observed in this study, however, this was not the case. The lack of increase in NO_2 was used to estimate first-order decay constants of $(2.0 \pm 1.0) \times 10^{-4}$ s^{-1} and $(2.75 \pm 1.25) \times 10^{-4}$ s^{-1} resulting in an effective lifetime of NO_2 of ~0.5-3 h. The loss of NO_2 at nighttime is presumably driven by deposition to soil and foliar surfaces since the lifetime of NO_2 towards its reactions with OH and O_3 at night is >28 and 14 h, respectively. By comparison, the daytime lifetime of NO_2 with respect to loss by reaction with OH is about 1 day. We conclude that the nighttime deposition of NO_2 is a major sink of boundary layer NO_x in this forested environment.

6   Data Availability:
All data can be found on https://across.aeris-data.fr/catalogue/.

7   Author contribution:
All authors contributed with measurements. Data analysis was conducted by STA with contributions from JNC and PD. CC and VM organized the field campaign with contributions from the individual group leads. STA and JNC developed the manuscript with contributions from all authors.

8   Competing Interests:
At least one of the (co-)authors is a member of the editorial board of Atmospheric Chemistry and Physics

9   Acknowledgements:
STA is thankful to the Alexander von Humboldt foundation for funding her stay at MPIC.

PD gratefully acknowledges the Deutsche Forschungsgemeinschaft (project "MONOTONS", project number: 522970430).

The ACROSS project has received funding from the French National Research Agency (ANR) under the investment program integrated into France 2030, with the reference ANR-17-MPGA-0002, and it was supported by the French National program LEFE (Les Enveloppes Fluides et l'Environnement) of the CNRS/INSU (Centre National de la Recherche Scientifique/Institut National des Sciences de l'Univers). Data from the ACROSS campaign are hosted by the French national center for Atmospheric data and services AERIS.

IMT Nord Europe acknowledges financial support from the CaPPA project, which is funded by the French National Research Agency (ANR) through the PIA (Programme d'Investissement d'Avenir) under contract ANR-11-LABX-0005-01, the Regional Council "Hauts-de-France" and the European Regional Development Fund (ERDF).

10 References:

Altimir, N., et al.: Foliage surface ozone deposition: a role for surface moisture?, Biogeosciences, 3, 209-228, 10.5194/bg-3-209-2006, 2006.

Breuninger, C., et al.: Field investigations of nitrogen dioxide (NO_2) exchange between plants and the atmosphere, Atmos. Chem. Phys., 13, 773-790, 10.5194/acp-13-773-2013, 2013.

Browne, E. C., et al.: Observations of total $RONO_2$ over the boreal forest: NO_x sinks and HNO_3 sources, Atmospheric Chemistry and Physics, 13, 4543-4562, 10.5194/acp-13-4543-2013, 2013.

Burkhardt, J. and Eiden, R.: Thin water films on coniferous needles: A new device for the study of water vapour condensation and gaseous deposition to plant surfaces and particle samples, Atmospheric Environment, 28, 2001-2011, https://doi.org/10.1016/1352-2310(94)90469-3, 1994.

Cantrell, C. and Michoud, V.: An Experiment to Study Atmospheric Oxidation Chemistry and Physics of Mixed Anthropogenic–Biogenic Air Masses in the Greater Paris Area, Bulletin of the American Meteorological Society, 103, 599-603, https://doi.org/10.1175/BAMS-D-21-0115.1, 2022.

Chaparro-Suarez, I. G., et al.: Nitrogen dioxide (NO2) uptake by vegetation controlled by atmospheric concentrations and plant stomatal aperture, Atmospheric Environment, 45, 5742-5750, https://doi.org/10.1016/j.atmosenv.2011.07.021, 2011.

Ciencewicki, J. and Jaspers, I.: Air Pollution and Respiratory Viral Infection, Inhalation Toxicology, 19, 1135-1146, 10.1080/08958370701665434, 2007.

Davidson, E. A. and Kingerlee, W.: A global inventory of nitric oxide emissions from soils, Nutrient Cycling in Agroecosystems, 48, 37-50, 10.1023/A:1009738715891, 1997.

Delaria, E. R. and Cohen, R. C.: A model-based analysis of foliar NOx deposition, Atmos. Chem. Phys., 20, 2123-2141, 10.5194/acp-20-2123-2020, 2020.

Delaria, E. R., et al.: Laboratory measurements of stomatal NO2 deposition to native California trees and the role of forests in the NOx cycle, Atmos. Chem. Phys., 20, 14023-14041, 10.5194/acp-20-14023-2020, 2020.

Delaria, E. R., et al.: Measurements of NO and NO_2 exchange between the atmosphere and Quercus agrifolia, Atmos. Chem. Phys., 18, 14161-14173, 10.5194/acp-18-14161-2018, 2018.

Dewald, P., et al.: Fate of the nitrate radical at the summit of a semi-rural mountain site in Germany assessed with direct reactivity measurements, Atmos. Chem. Phys., 22, 7051-7069, 10.5194/acp-22-7051-2022, 2022.

Draxler, R. R. and Rolph, G. D.: HYSPLIT (HYbrid Single-Particle Lagrangian Integrated Trajectory) Model access via NOAA ARL READY Website (http://ready.arl.noaa.gov/HYSPLIT.php). NOAA Air Resources Laboratory, Silver Spring, MD., 2011.

Elshorbany, Y. F., et al.: Impact of HONO on global atmospheric chemistry calculated with an empirical parameterization in the EMAC model, Atmos. Chem. Phys., 12, 9977-10000, 10.5194/acp-12-9977-2012, 2012.

Emberson, L. D., et al.: Ozone effects on crops and consideration in crop models, European Journal of Agronomy, 100, 19-34, https://doi.org/10.1016/j.eja.2018.06.002, 2018.

Farmer, D. K. and Cohen, R. C.: Observations of HNO_3, ΣAN, ΣPN and NO_2 fluxes: evidence for rapid HO_x chemistry within a pine forest canopy, Atmos. Chem. Phys., 8, 3899-3917, 10.5194/acp-8-3899-2008, 2008.

Finkelstein, P. L., et al.: Ozone and sulfur dioxide dry deposition to forests: Observations and model evaluation, Journal of Geophysical Research: Atmospheres, 105, 15365-15377, https://doi.org/10.1029/2000JD900185, 2000.

Friedrich, N., et al.: Measurement of NOx and NOy with a thermal dissociation cavity ring-down spectrometer (TD-CRDS): instrument characterisation and first deployment, Atmos. Meas. Tech., 13, 5739-5761, 10.5194/amt-13-5739-2020, 2020.

Ganzeveld, L. and Lelieveld, J.: Dry deposition parameterization in a chemistry general circulation model and its influence on the distribution of reactive trace gases, Journal of Geophysical Research: Atmospheres, 100, 20999-21012, https://doi.org/10.1029/95JD02266, 1995.

Gessler, A., et al.: NH3 and NO2 fluxes between beech trees and the atmosphere – correlation with climatic and physiological parameters, New Phytologist, 147, 539-560, https://doi.org/10.1046/j.1469-8137.2000.00712.x, 2000.

Geyer, A. and Stutz, J.: Vertical profiles of NO_3, N_2O_5, O_3, and NOx in the nocturnal boundary layer: 2. Model studies on the altitude dependence of composition and chemistry (vol 109, art no D16399, 2004), Journal of Geophysical Research-Atmospheres, 109, 10.1029/2004JD005217 2004.

Hallquist, M., et al.: The formation, properties and impact of secondary organic aerosol: current and emerging issues, Atmospheric Chemistry and Physics, 9, 5155-5236, 10.5194/acp-9-5155-2009, 2009.

Heland, J., et al.: A new instrument to measure gaseous nitrous acid (HONO) in the atmosphere, Environmental Science & Technology, 35, 3207-3212, DOI 10.1021/es000303t, 2001.

Hens, K., et al.: Observation and modelling of HOx radicals in a boreal forest, Atmospheric Chemistry and Physics, 14, 8723-8747, 10.5194/acp-14-8723-2014, 2014.

Horii, C. V., et al.: Fluxes of nitrogen oxides over a temperate deciduous forest, Journal of Geophysical Research: Atmospheres, 109, https://doi.org/10.1029/2003JD004326, 2004.

IUPAC Task Group on Atmospheric Chemical Kinetic Data Evaluation, (Ammann, M., Cox, R.A., Crowley, J.N., Herrmann, H., Jenkin, M.E., McNeill, V.F., Mellouki, A., Rossi, M. J., Troe, J. and Wallington, T. J.). Last access April. 2024: https://iupac.aeris-data.fr/, last

Jaeglé, L., et al.: Global partitioning of NOx sources using satellite observations: Relative roles of fossil fuel combustion, biomass burning and soil emissions, Faraday Discussions, 130, 407-423, 10.1039/B502128F, 2005.

Kanakidou, M., et al.: Organic aerosol and global climate modelling: a review, Atmospheric Chemistry and Physics, 5, 1053-1123, 10.5194/acp-5-1053-2005, 2005.

Kane, S. M., et al.: Heterogeneous uptake of gaseous N_2O_5 by $(NH_4)_2SO_4$, NH_4HSO_4, and H_2SO_4 aerosols, Journal of Physical Chemistry a, 105, 6465-6470, 2001.

Kiendler-Scharr, A., et al.: Ubiquity of organic nitrates from nighttime chemistry in the European submicron aerosol, Geophysical Research Letters, 43, 7735-7744, 10.1002/2016gl069239, 2016.

Kleffmann, J., et al.: Intercomparison of the DOAS and LOPAP techniques for the detection of nitrous acid (HONO), Atmospheric Environment, 40, 3640-3652, https://doi.org/10.1016/j.atmosenv.2006.03.027, 2006.

Kukui, A., et al.: Chemical ionisation mass spectrometer for measurements of OH and Peroxy radical concentrations in moderately polluted atmospheres, Journal of Atmospheric Chemistry, 61, 133-154, 10.1007/s10874-009-9130-9, 2008.

Kurpius, M. R. and Goldstein, A. H.: Gas-phase chemistry dominates O_3 loss to a forest, implying a source of aerosols and hydroxyl radicals to the atmosphere, Geophysical Research Letters, 30, 10.1029/2002gl016785, 2003.

Liebmann, J., et al.: Alkyl nitrates in the boreal forest: formation via the NO3-, OH- and O3-induced oxidation of biogenic volatile organic compounds and ambient lifetimes, Atmos. Chem. Phys., 19, 10391-10403, 10.5194/acp-19-10391-2019, 2019.

Liebmann, J. M., et al.: Direct measurements of NO3 reactivity in and above the boundary layer of a mountaintop site: identification of reactive trace gases and comparison with OH reactivity, Atmospheric Chemistry and Physics, 18, 12045-12059, 10.5194/acp-18-12045-2018, 2018.

Lightfoot, P. D., et al.: Organic peroxy radicals - kinetics, spectroscopy and tropospheric chemistry, Atmospheric Environment, Part A: General Topics, 26, 1805-1961, 1992.

Meusel, H., et al.: Daytime formation of nitrous acid at a coastal remote site in Cyprus indicating a common ground source of atmospheric HONO and NO, Atmospheric Chemistry and Physics, 16, 14475-14493, 10.5194/acp-16-14475-2016, 2016.

Padro, J.: Seasonal contrasts in modelled and observed dry deposition velocities of O3, SO2 and NO2 over three surfaces, Atmospheric Environment. Part A. General Topics, 27, 807-814, https://doi.org/10.1016/0960-1686(93)90002-G, 1993.

Padro, J.: Summary of ozone dry deposition velocity measurements and model estimates over vineyard, cotton, grass and deciduous forest in summer, Atmospheric Environment, 30, 2363-2369, https://doi.org/10.1016/1352-2310(95)00352-5, 1996.

Phillips, G. J., et al.: The detection of nocturnal N_2O_5 as HNO_3 by alkali- and aqueous-denuder techniques, Atmospheric measurement techniques, 6, 231-237, 10.5194/amt-6-231-2013, 2013.

Phillips, G. J., et al.: Significant concentrations of nitryl chloride observed in rural continental Europe associated with the influence of sea salt chloride and anthropogenic emissions, Geophysical Research Letters, 39, L10811, doi:10.1029/2012GL051912, 2012.

Pilegaard, K.: Processes regulating nitric oxide emissions from soils, Philosophical Transactions of the Royal Society B-Biological Sciences, 368, ARTN 20130126

10.1098/rstb.2013.0126, 2013.

Pilegaard, K., et al.: Factors controlling regional differences in forest soil emission of nitrogen oxides (NO and N_2O), Biogeosciences, 3, 651-661, 10.5194/bg-3-651-2006, 2006.

697   Puxbaum, H. and Gregori, M.: Seasonal and annual deposition rates of sulphur, nitrogen and
698   chloride species to an oak forest in north-eastern austria (wolkersdorf, 240 m a.s.l.), Atmos.
699   Env., 32, 3557-3568, https://doi.org/10.1016/S1352-2310(98)00073-9, 1998.
700   Rannik, Ü., et al.: Ozone deposition into a boreal forest over a decade of observations: evaluating
701   deposition partitioning and driving variables, Atmos. Chem. Phys., 12, 12165-12182,
702   10.5194/acp-12-12165-2012, 2012.
703   Romer Present, P. S., et al.: The changing role of organic nitrates in the removal and transport of
704   NOx, Atmos. Chem. Phys. Discuss., 2019, 1-18, 10.5194/acp-2019-471, 2019.
705   Rondón, A., et al.: Dry deposition of nitrogen dioxide and ozone to coniferous forests, Journal of
706   Geophysical Research: Atmospheres, 98, 5159-5172, https://doi.org/10.1029/92JD02335,
707   1993.
708   Rosenkranz, P., et al.: Soil N and C trace gas fluxes and microbial soil N turnover in a sessile oak
709   (Quercus petraea (Matt.) Liebl.) forest in Hungary, Plant and Soil, 286, 301-322,
710   10.1007/s11104-006-9045-z, 2006.
711   Schindlbacher, A., et al.: Effects of soil moisture and temperature on NO, NO_2, and N_2O
712   emissions from European forest soils, Journal of Geophysical Research: Atmospheres, 109,
713   https://doi.org/10.1029/2004JD004590, 2004.
714   Schumann, U. and Huntrieser, H.: The global lightning-induced nitrogen oxides source, Atmos.
715   Chem. Phys., 7, 3823-3907, 10.5194/acp-7-3823-2007, 2007.
716   Shepson, P. B., et al.: Determination of the relative ozone and PAN deposition velocities at night,
717   Geophysical Research Letters, 19, 1121-1124, 10.1029/92gl01118, 1992.
718   Sobanski, N., et al.: A five-channel cavity ring-down spectrometer for the detection of NO_2, NO_3,
719   N_2O_5, total peroxy nitrates and total alkyl nitrates, Atmospheric Measurement Techniques, 9,
720   5103-5118, 10.5194/amt-9-5103-2016, 2016.
721   Stutz, J., et al.: Vertical profiles of NO_3, N_2O_5, O_3, and NO_X in the nocturnal boundary layer: 1.
722   Observations during the Texas Air Quality Study 2000 Journal of Geophysical Research-
723   Atmospheres, 109, art. D12306, 10.1029/2003JD004209, 2004.
724   Thoene, B., et al.: Absorption of atmospheric NO2 by spruce (Picea abies) trees, New Phytologist,
725   134, 257-266, https://doi.org/10.1111/j.1469-8137.1996.tb04630.x, 1996.
726   Val Martin, M., et al.: Large-scale impacts of anthropogenic pollution and boreal wildfires on the
727   nitrogen oxides over the central North Atlantic region, Journal of Geophysical Research:
728   Atmospheres, 113, https://doi.org/10.1029/2007JD009689, 2008.
729   Weber, P. and Rennenberg, H.: Dependency of nitrogen dioxide (NO2) fluxes to wheat (Triticum
730   aestivum L.) leaves from NO2 concentration, light intensity, temperature and relative humidity
731   determined from controlled dynamic chamber experiments, Atmospheric Environment, 30,
732   3001-3009, https://doi.org/10.1016/1352-2310(96)00008-8, 1996.
733   Wu, Z., et al.: Dry deposition of O3 and SO2 estimated from gradient measurements above a
734   temperate mixed forest, Environmental Pollution, 210, 202-210,
735   https://doi.org/10.1016/j.envpol.2015.11.052, 2016.
736   Zhou, P., et al.: Simulating ozone dry deposition at a boreal forest with a multi-layer canopy
737   deposition model, Atmos. Chem. Phys., 17, 1361-1379, 10.5194/acp-17-1361-2017, 2017.

738

739   **11 Figures:**
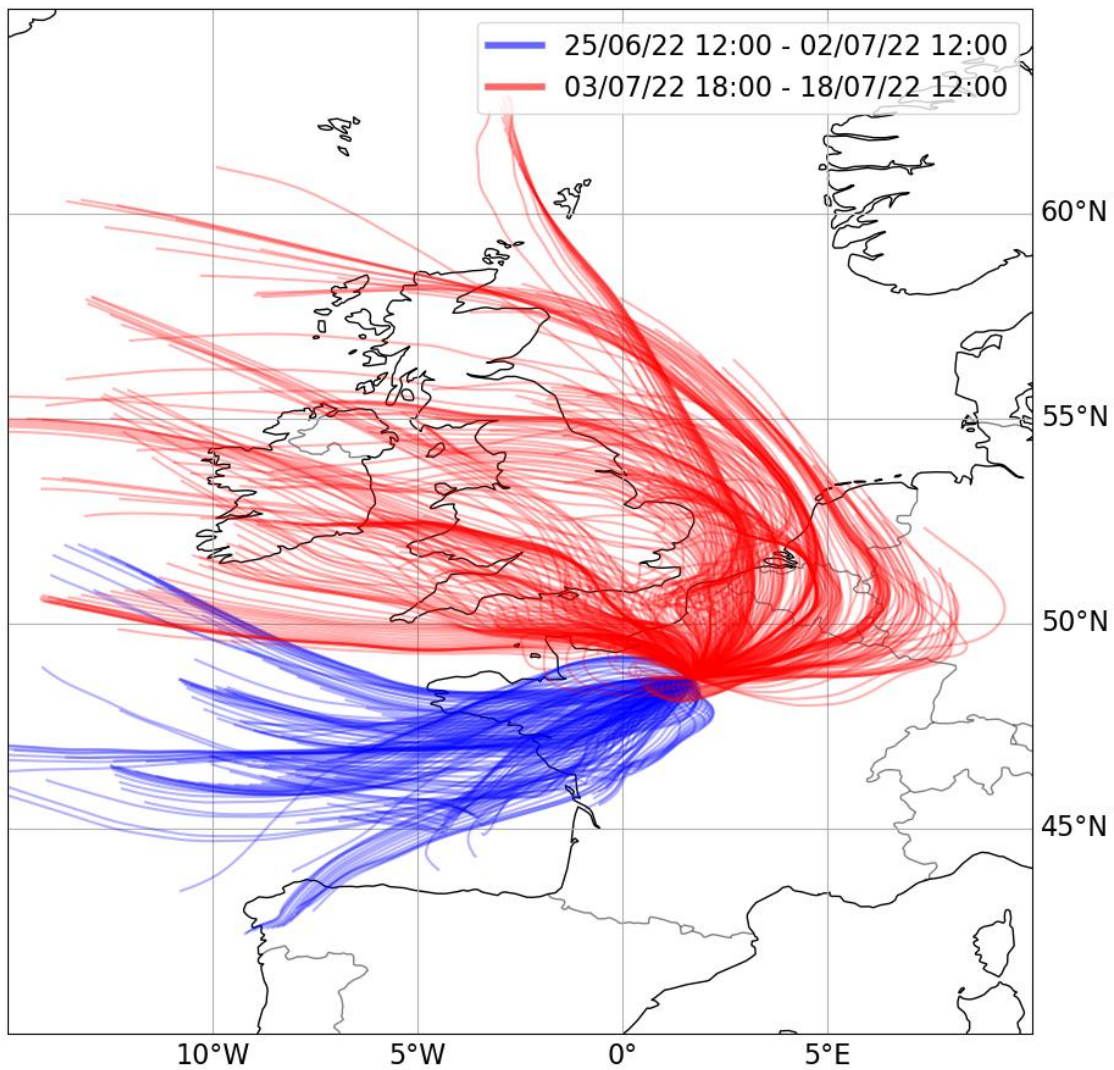
740

741   Figure 1: 48-hour back trajectories from the Rambouillet forest supersite using the Hybrid Single-
742   Particle Lagrangian Integrated Trajectory model (HYSPLIT, version 4, 2019).
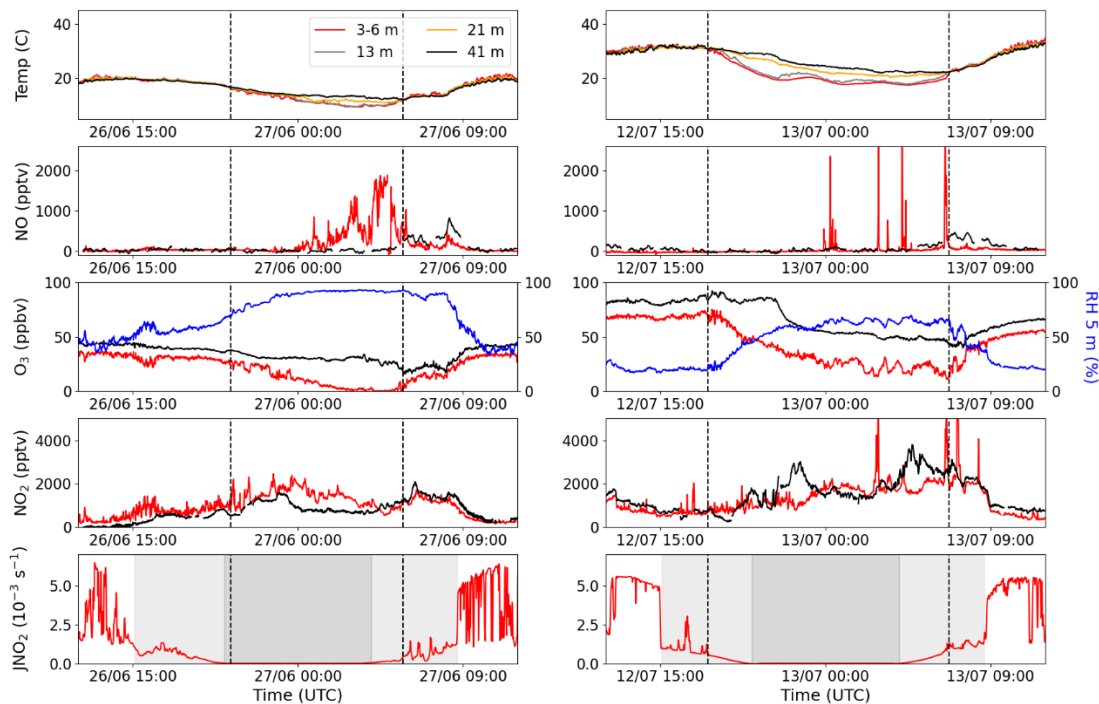
Figure 2: Measurements of temperature, NO, O_3, RH, NO_2, and JNO_2 for two different nights during the campaign; one during the Atlantic phase (left panels) and one during the continental phase (right panels). The different colours symbolize four different heights; red = 3-6 m, grey = 13 m, orange = 21 m, and black = 41 m, and the blue shows the RH at 5 m. The grey shaded areas in the JNO_2 plots shows the time the MPIC container was in shade during the afternoon and morning (light grey) and nighttime (dark grey). The vertical black dashed lines indicate the beginning and end of the observed temperature inversions in the top panels.
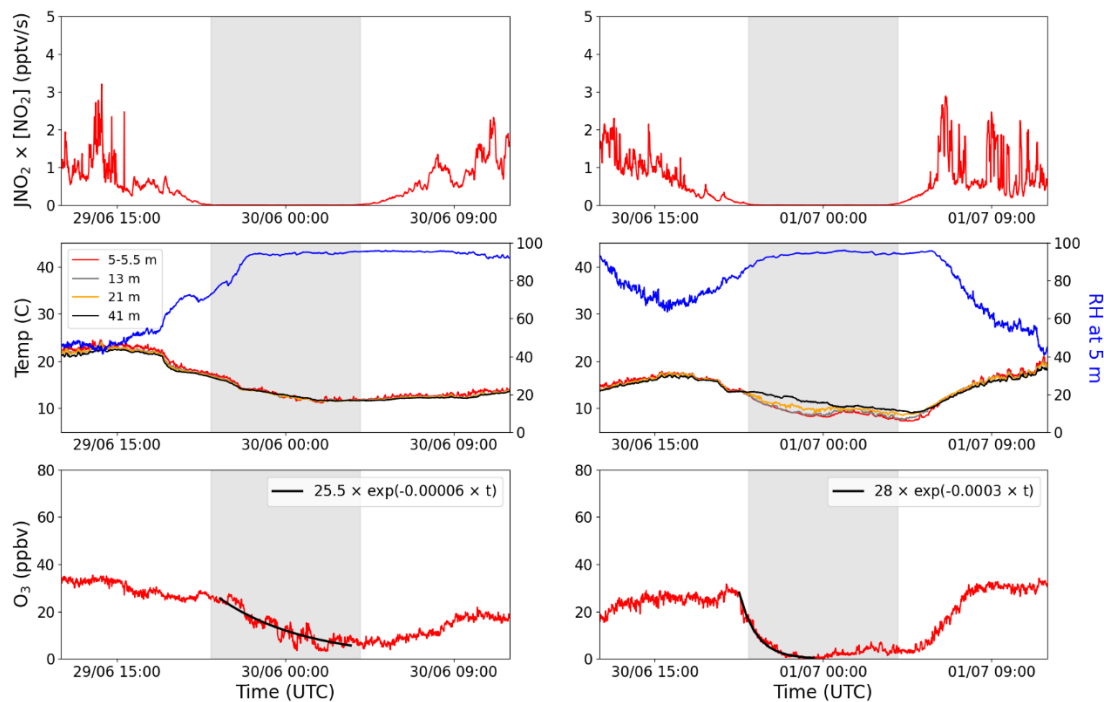
752

753 Figure 3: The production of O_3 ($JNO_2 \times [NO_2]$), temperature, RH, and O_3 plotted for two nights
754 with high average RH; one without a temperature inversion (left panels) and one with a
755 temperature inversion (right panels). The different colours symbolize four different heights; red =
756 5-5.4 m, grey = 13 m, orange = 21 m, and black = 41 m, and the blue shows the RH at 5 m. The
757 net nighttime O_3 loss is fitted with an exponential decay curve (solid black line) in the bottom
758 plots. The grey shaded areas represent the nighttime.

759
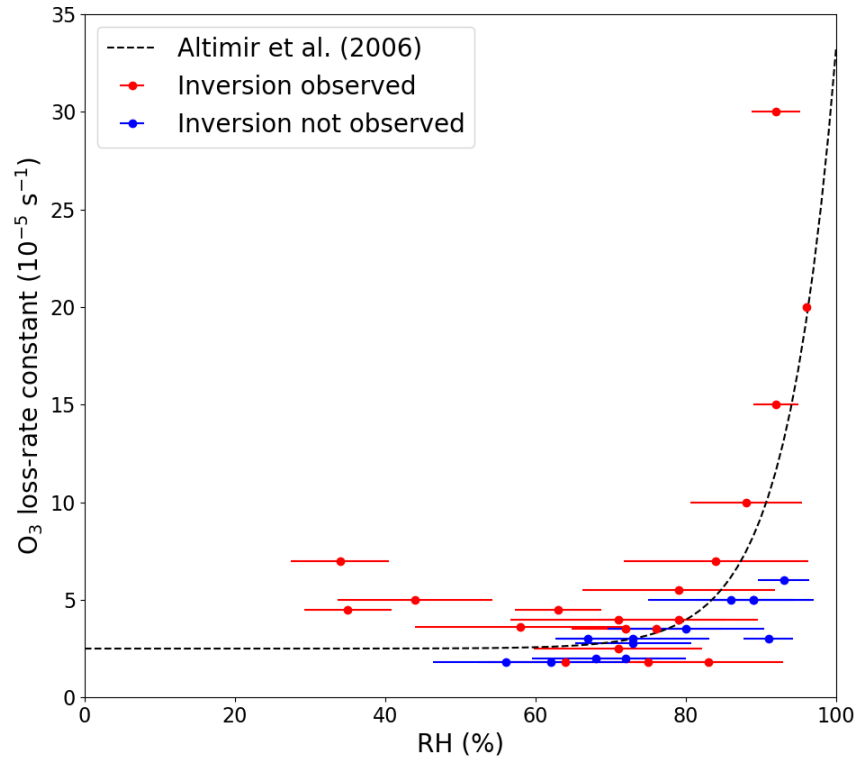
760

761 Figure 4: Net O_3 loss-rate constants at 5.4 m plotted against the average relative humidity measured
762 during the time used to fit the exponential decay of O_3. The error bars represent ±1σ on the average
763 RH. The dashed line symbolizes the observations made by Altimir et al. (2006).

764
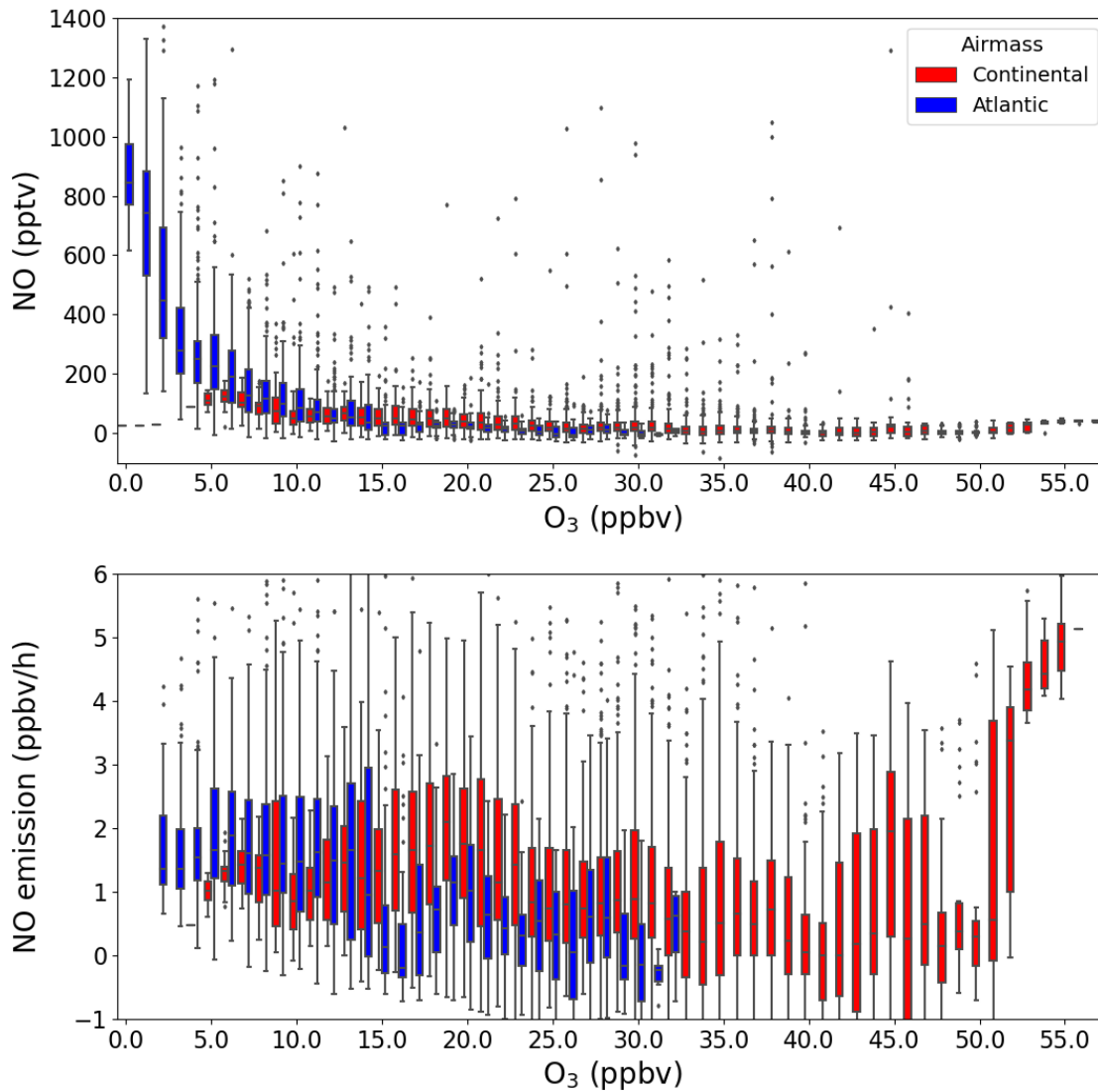
Figure 5: NO (top) and NO emission (bottom) plotted against O_3 in a box-and-whiskers plot, where the outliers are defined as being outside $1.5 \times$ IQR. The colours represent the two different air masses.

768

769
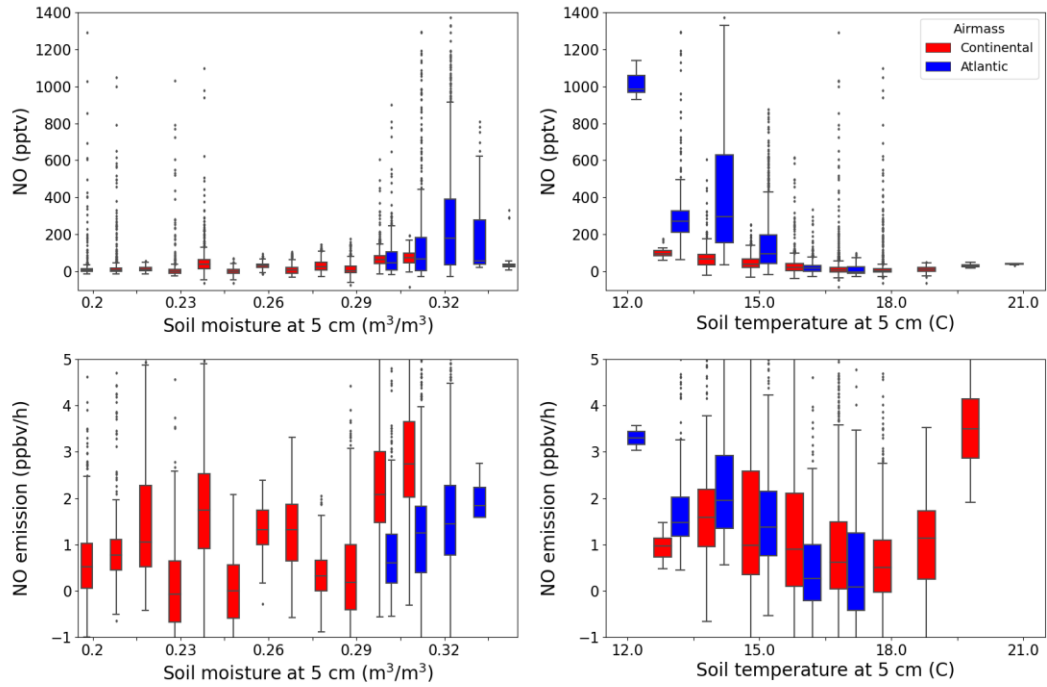
Figure 6: NO (top panels) and NO emission (bottom panels) plotted against soil moisture (left panels) and temperature (right panels) at 5 cm below the surface in a box-and-whiskers plot, where the outliers are defined as being outside $1.5 \times$ IQR. The colours represent the two different air masses.

774

775
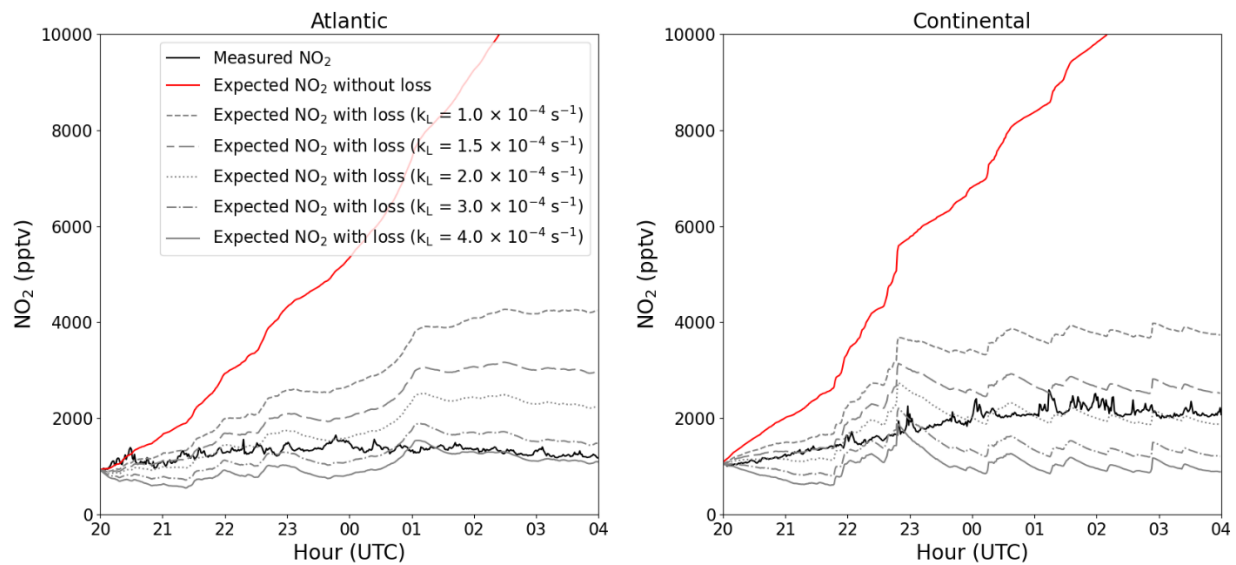
Figure 7: Average nighttime profiles of NO_2 at 5.4 m for each of the two phases (black) plotted
together with the expected NO_2 with (grey) and without (red) NO_2 loss.

778
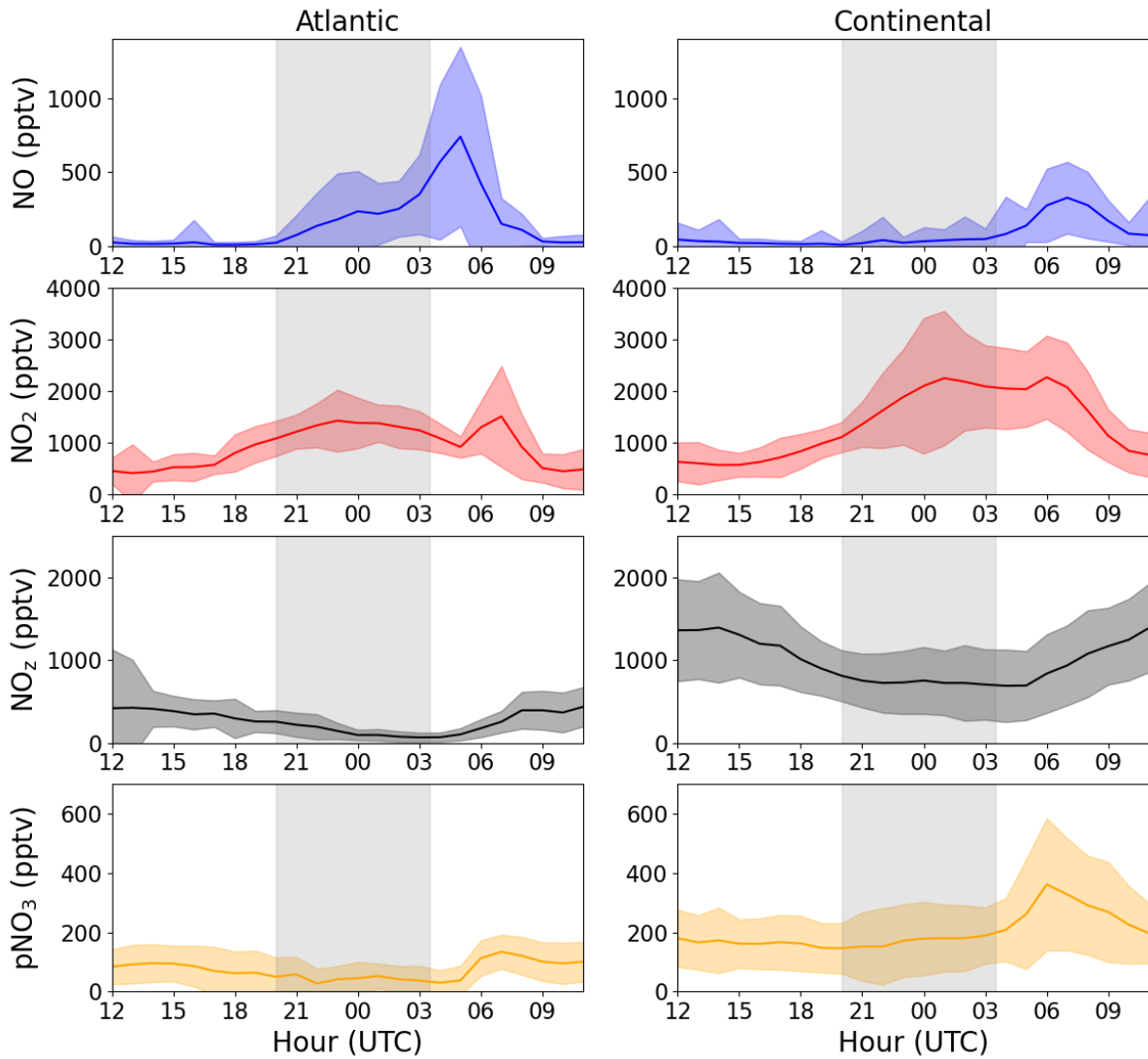
Figure 8: Average diel profiles of NO, NO₂, total gas-phase NO$_z$, and particulate nitrate (pNO₃) at
3-6 m above ground for the Atlantic (left panels) and Continental (right panels) phases. The grey
shaded areas symbolize nighttime.

782 **12 Tables:**
783

784 Table 1: Measured NO soil emission in European forests with the same tree types as in the
785 Rambouillet forest.

Dominant tree type	Location	NO emission (μg N m^{-2} h^{-1})	Reference
Oak	Matra Mountains, Hungary	2.1 6.0 $\pm$ 3.3 (summer) 8.4 $\pm$ 2.4 (autumn)	(Pilegaard et al., 2006) (Rosenkranz et al., 2006) (Rosenkranz et al., 2006)
Pine	San Rossore, Italy	5.4	(Pilegaard et al., 2006)
Beech	Schottenwald, Austria	25.5 $\pm$ 7.5 4.2	(Schindlbacher et al., 2004) (Pilegaard et al., 2006)
Beech	Klausen-Leopolsdorf, Austria	10.2 $\pm$ 3.4 0.7	(Schindlbacher et al., 2004) (Pilegaard et al., 2006)
Spruce-Fir-Beech	Achenkirch, Austria	2.8 $\pm$ 1.4 0.9	(Schindlbacher et al., 2004) (Pilegaard et al., 2006)
Mixed deciduous	Ticino Park, Italy	18.5 $\pm$ 5.8 Below LOD	(Schindlbacher et al., 2004) (Pilegaard et al., 2006)

786

787